



# The Dust-to-gas Ratio and the Role of Radiation Pressure in Luminous, Obscured Quasars

Hyunsung D. Jun<sup>1</sup> , Roberto J. Assef<sup>2</sup> , Christopher M. Carroll<sup>3</sup> , Ryan C. Hickox<sup>3</sup> , Yonghwi Kim<sup>1</sup> , Jaehyun Lee<sup>1</sup> ,  
Claudio Ricci<sup>2,4</sup> , and Daniel Stern<sup>5</sup>

<sup>1</sup> School of Physics, Korea Institute for Advanced Study, 85 Hoegiro, Dongdaemun-gu, Seoul 02455, Republic of Korea; [hsjun@kias.re.kr](mailto:hsjun@kias.re.kr)

<sup>2</sup> Núcleo de Astronomía de la Facultad de Ingeniería y Ciencias, Universidad Diego Portales, Av. Ejército Libertador 441, Santiago, Chile

<sup>3</sup> Department of Physics & Astronomy, Dartmouth College, Hanover, NH 03755, USA

<sup>4</sup> Kavli Institute for Astronomy and Astrophysics, Peking University, Beijing 100871, People's Republic of China

<sup>5</sup> Jet Propulsion Laboratory, California Institute of Technology, 4800 Oak Grove Drive, Pasadena, CA 91109, USA

Received 2020 August 17; revised 2020 October 28; accepted 2020 October 28; published 2020 December 31

## Abstract

The absence of high-Eddington-ratio, obscured active galactic nuclei (AGNs) in local ( $z \lesssim 0.1$ ) samples of moderate-luminosity AGNs has generally been explained to result from radiation pressure on the dusty gas governing the level of nuclear ( $\lesssim 10$  pc) obscuration. However, very high accretion rates are routinely reported among obscured quasars at higher luminosities and may require a different feedback mechanism. We compile constraints on obscuration and Eddington ratio for samples of X-ray, optical, infrared, and submillimeter selected AGNs at quasar luminosities. Whereas moderate-luminosity, obscured AGNs in the local universe have a range of lower Eddington ratios ( $f_{\text{Edd}} \sim 0.001\text{--}0.1$ ), the most luminous ( $L_{\text{bol}} \gtrsim 10^{46}$  erg s<sup>−1</sup>) IR/submillimeter-bright, obscured quasars out to  $z \sim 3$  commonly have very high Eddington ratios ( $f_{\text{Edd}} \sim 0.11$ ). This apparent lack of radiation-pressure feedback in luminous, obscured quasars is likely coupled with AGN timescales, such that a higher fraction of luminous, obscured quasars are seen because of the short timescale for which quasars are most luminous. When adopting quasar evolutionary scenarios, extended ( $\sim 10^{2-3}$  pc) obscuration may work together with the shorter timescales to explain the observed fraction of obscured, luminous quasars, while outflows driven by radiation pressure will slowly clear this material over the AGN lifetime.

*Unified Astronomy Thesaurus concepts:* Active galaxies (17); Galaxy evolution (594); Quasars (1319); Interstellar medium (847)

## 1. Introduction

Accretion rate and obscuration of active galactic nuclei (AGNs) are two fundamental parameters that explain their diverse observed properties (e.g., Shen & Ho 2014; Hickox & Alexander 2018). According to AGN evolutionary scenarios (e.g., Hopkins et al. 2008; Hickox et al. 2009), matter falling onto the black hole (BH) will trigger AGN activity at various strengths depending on the environment, which in turn will heat and sweep any potential obscuring circumnuclear material. Thus, feeding onto the BH and feedback from the AGN are closely related on the obscuration–accretion rate plane.

Ricci et al. (2017c, hereafter R17c) recently reported on a study of the relationship between obscuration and accretion rate in a large, relatively unbiased, and complete sample of local AGNs. Specifically, they investigated 836 AGNs with a median redshift of  $\langle z \rangle = 0.037$  selected by the hard X-ray (14–195 keV) Swift Burst Alert Telescope (BAT; Gehrels et al. 2004; Barthelmy et al. 2005; Krimm et al. 2013) all-sky survey (Baumgartner et al. 2013; Koss et al. 2017; Oh et al. 2018), which is sensitive to sources with column densities up to  $N_{\text{H}} \approx 10^{24}$  cm<sup>−2</sup>. Approximately one-half of the sources had robust measurements of column densities, intrinsic X-ray luminosities, and black hole masses, from which R17c was able to show that while unobscured AGNs are seen with Eddington fractions up to the Eddington limit, very few local, obscured AGNs are found with Eddington fractions above approximately 10%. This strengthened earlier results based on smaller samples (e.g., Fabian et al. 2009) and was interpreted as evidence for radiation-pressure-driven AGN feedback (e.g., King 2003; Murray et al. 2005) clearing the immediate BH

environment of dusty gas (e.g., Fabian et al. 2006, 2008). For dusty gas (neutral or partially ionized), the effective cross section between matter and radiation ( $\sigma_{\text{dust}}$ ) becomes larger than that between electrons and radiation for ionized gas ( $\sigma_{\text{T}}$ , for Thompson scattering), due to absorption of radiation by dust. This is given by the Eddington ratio for ionized gas,

$$\begin{aligned} f_{\text{Edd}} &= L_{\text{bol}}/L_{\text{Edd}} \\ L_{\text{Edd}} &= 4\pi GM_{\text{BH}}m_{\text{p}}c/\sigma_{\text{T}}, \end{aligned} \quad (1)$$

where  $L_{\text{bol}}$  is the bolometric luminosity,  $L_{\text{Edd}}$  is the Eddington luminosity with  $M_{\text{BH}}$  the BH mass, and  $m_{\text{p}}$  is the proton mass. For dusty gas, we use  $\sigma_{\text{dust}}$  instead of  $\sigma_{\text{T}}$  in Equation (1), where  $f_{\text{Edd}}$  is redefined as the effective Eddington ratio ( $f_{\text{Edd,dust}} = f_{\text{Edd}}\sigma_{\text{dust}}/\sigma_{\text{T}}$ ). AGNs are strong ionizing sources, but they are fully ionized close to their accretion disks (e.g., Osterbrock 1979; Ballantyne et al. 2001), though the greater than parsec-scale environment starts to be composed of dusty gas (e.g., Kishimoto et al. 2011; Minezaki et al. 2019).

To visualize how the radiation pressure would blow away the nuclear material, we plot  $f_{\text{Edd}}$  where  $f_{\text{Edd,dust}} = 1$  as a function of  $N_{\text{H}}$  in Figure 1, adopted from Fabian et al. (2009).<sup>6</sup> When AGNs are obscured beyond the typical  $N_{\text{H}} \sim 10^{22}$  cm<sup>−2</sup> value for galaxies (e.g., Buchner & Bauer 2017; Hickox & Alexander 2018),  $f_{\text{Edd}}(f_{\text{Edd,dust}} = 1)$  is on the order of 0.01–0.1, and the accretion becomes super-Eddington (shaded region)

<sup>6</sup> We note that at  $N_{\text{H}} \gtrsim 10^{24}$  cm<sup>−2</sup>,  $f_{\text{Edd,dust}} < f_{\text{Edd}}$ , or the radiation pressure on dusty gas is weaker than on ionized gas. Only because of the relative lack of super-Eddington gas accretion, we restrict the  $f_{\text{Edd}}(f_{\text{Edd,dust}} = 1)$  curve to  $f_{\text{Edd}} < 1$  throughout.

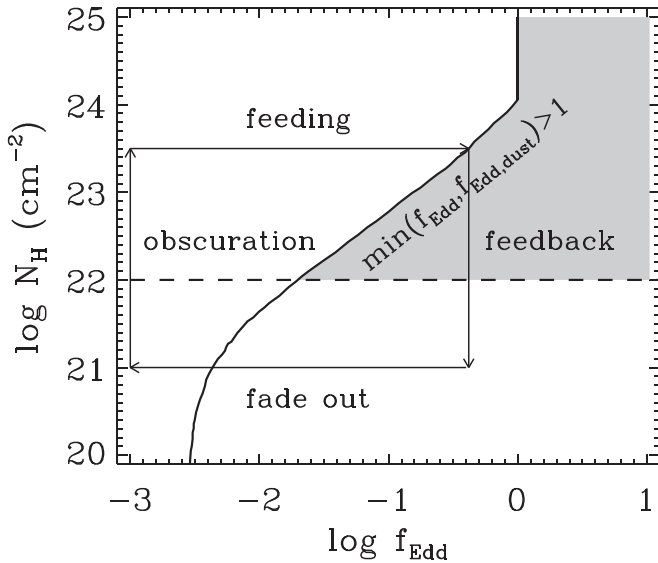


**Figure 1.** The  $N_{\text{H}}-f_{\text{Edd}}$  plane showing a schematic evolution of local AGNs probed by the Swift/BAT X-ray data (R17c). The shaded region indicates the region unoccupied in R17c, which is explained as radiation pressure quickly blowing out the nuclear obscuration composed of dusty gas. In this view, the nuclear obscuration is followed by feeding of gas onto supermassive BHs, where the obscuration is suppressed by radiation-pressure-driven feedback until the accretion starves and the AGN fades out.

even if  $f_{\text{Edd}}(f_{\text{Edd,dust}} = 1) < f_{\text{Edd}} < 1$ . This makes it easier for radiation pressure to blow out the dusty nuclear gas on the order of 1–10 pc (e.g., Jaffe et al. 2004; Ramos Almeida & Ricci 2017; Ichikawa et al. 2019) and matches well with the observations of R17c reporting a lack of AGNs with  $f_{\text{Edd,dust}} > 1$ , perhaps favoring an episodic nuclear obscuration and blowout governed by radiation pressure.

The largest limitation for the Swift/BAT survey, which is relatively unbiased and complete for local AGNs, is that its shallow sensitivity misses luminous quasars in the distant universe. Here, we explore high-luminosity/redshift samples of optical quasars (e.g., Schneider et al. 2010), optical–IR red quasars with large color excess, where  $E(B - V) \lesssim 1.5$  mag (e.g., Glikman et al. 2007; Banerji et al. 2012; Ross et al. 2015; Hamann et al. 2017), dust-obscured galaxies (DOGs, Dey et al. 2008; Hot DOGs, Eisenhardt et al. 2012), and submillimeter galaxies (SMGs, Blain et al. 2002), where the latter two are likely subsets and distant analogs of local ultraluminous infrared galaxies (ULIRGs,  $\log L_{\text{IR}} > 10^{12} L_{\odot}$ ; Sanders et al. 1988) and their higher-luminosity cousins (e.g., hyLIRGs, Sanders & Mirabel 1996; ELIRGs, Tsai et al. 2015). We also add the highest-obscuration, Compton-thick AGNs, that is, AGNs with X-ray-obscuring column densities of  $N_{\text{H}} \gtrsim 10^{24} \text{ cm}^{-2}$ , observed with NuSTAR (Harrison et al. 2013).

The latest studies of obscured quasars with large  $E(B - V)$  values, through careful analysis to quantify and minimize the effect of obscuration, have reported near-Eddington to Eddington-limited accretion ( $f_{\text{Edd}} \sim 0.1$ –1, e.g., Alexander et al. 2008; Urrutia et al. 2012; Kim et al. 2015; Assef et al. 2020; Jun et al. 2020). Furthermore, Glikman (2017a) and Lansbury et al. (2020) find many obscured quasars with  $f_{\text{Edd,dust}} > 1$  at high  $N_{\text{H}}$ . These observations suggest that radiation pressure on dusty gas is effective, but is potentially less effective for obscured, luminous quasars since the length of time that luminous quasars are active is shorter than the length of time that less-luminous AGNs are

active (e.g., Hopkins et al. 2005, 2006). Alternatively, luminous, obscured quasars are thought to be observed in a short phase in which they are blowing out the material through outflows stronger at higher luminosities (e.g., LaMassa et al. 2017; Perrotta et al. 2019; Temple et al. 2019; Jun et al. 2020), perhaps requiring a different nuclear or galactic environment from less-luminous, obscured AGNs. Hence, there is growing interest in which AGN property drives radiation-pressure feedback, and in which temporal and spatial scales it is effective.

In this work, we attempt to constrain the  $N_{\text{H}}-f_{\text{Edd}}$  and  $E(B - V)-f_{\text{Edd}}$  planes for quasars from multiwavelength AGN samples (Section 2) and through a consistent method to estimate  $N_{\text{H}}$ ,  $E(B - V)$  (Section 3), and  $f_{\text{Edd}}$  values (Section 4). We present (Section 5) and discuss (Section 6) the  $N_{\text{H}}-f_{\text{Edd}}$  and  $E(B - V)-f_{\text{Edd}}$  distributions for quasars in terms of various feedback mechanisms. Throughout, including the luminosities from the literature, we use a flat  $\Lambda$ CDM cosmology with  $H_0 = 70 \text{ km s}^{-1} \text{ Mpc}^{-1}$ ,  $\Omega_m = 0.3$ , and  $\Omega_{\Lambda} = 0.7$ .

## 2. The Sample

Probing the distribution of  $N_{\text{H}}-f_{\text{Edd}}$  and  $E(B - V)-f_{\text{Edd}}$  values from a statistically complete AGN sample is complicated for several reasons. AGNs radiate across almost the entire electromagnetic spectrum, but show a wide range of spectral energy distributions (SEDs) due to physical processes governing the radiation, host galaxy contamination, and obscuration on various scales around the accreting BHs (e.g., Lansbury et al. 2017; Hickox & Alexander 2018). Therefore, we found it beneficial to compile quasar samples selected at various wavelengths over a wide range of luminosity and redshift. Still, we chose to add only the data from the literature that meaningfully increase the sample size for a given wavelength selection.

In Figure 2 we plot the AGN samples from X-ray, optically blue, optical–IR red, and IR/submillimeter-bright populations, also summarized in Table 1. At  $z < 0.3$ , the Swift/BAT AGN in R17c (with  $N_{\text{H}}$  from Ricci et al. 2017d;  $E(B - V)$  from Koss et al. 2017) has the advantage of minimal obscuration bias from the hard X-ray selection and covers a wide range of luminosities, reaching down to low-luminosity AGNs and up to quasar luminosities ( $10^{41} \lesssim L_{\text{bol}} \lesssim 10^{47} \text{ erg s}^{-1}$ ). However, the Swift/BAT survey lacks the sensitivity to probe the distant or luminous AGN populations marked in Figure 2. We complemented the highest obscurations using Compton-thick ( $N_{\text{H}} \gtrsim 10^{24} \text{ cm}^{-2}$ ) AGNs observed with NuSTAR (B15b; B16) and the higher luminosities/redshifts from optical Sloan Digital Sky Survey (SDSS) quasars (e.g., Schneider et al. 2010;  $N_{\text{H}}$  from Y09;  $E(B - V)$  from J13), red quasars (L16, originally from Glikman et al. 2012; K18, averaged between Glikman et al. 2007 and Urrutia et al. 2009), and quasars from ULIRGs (broad-line<sup>7</sup> ULIRGs in A08, with  $N_{\text{H}}$  from Severgnini et al. 2001).

We further include  $z > 0.3$  quasars to search for luminous quasars, adding type 1 quasars from the SDSS (i.e., WISSH quasars,  $N_{\text{H}}$  from M17 and  $E(B - V)$  from V18b) and a variety of quasars with red optical-to-infrared colors, that is, heavily reddened quasars (B12; B13; B15a; T19), red quasars (U12; G17; L17; K18), extremely red quasars (P19 with  $N_{\text{H}}$  from G18 and  $E(B - V)$  from Hamann et al. 2017), and DOGs (C16; T20).

<sup>7</sup> Throughout, we classify narrow-line AGNs to be type  $\geq 1.8$  (weak broad  $\text{H}\alpha$  and  $\text{H}\beta$ ,  $[\text{O III}]/\text{H}\beta > 3$ , Winkler 1992), and broad-line AGNs to be type  $\leq 1.5$  (comparable broad-to-narrow  $\text{H}\beta$  and  $[\text{O III}]/\text{H}\beta < 3$ ). When the AGN types are not specified, we follow the visual classifications from the literature.

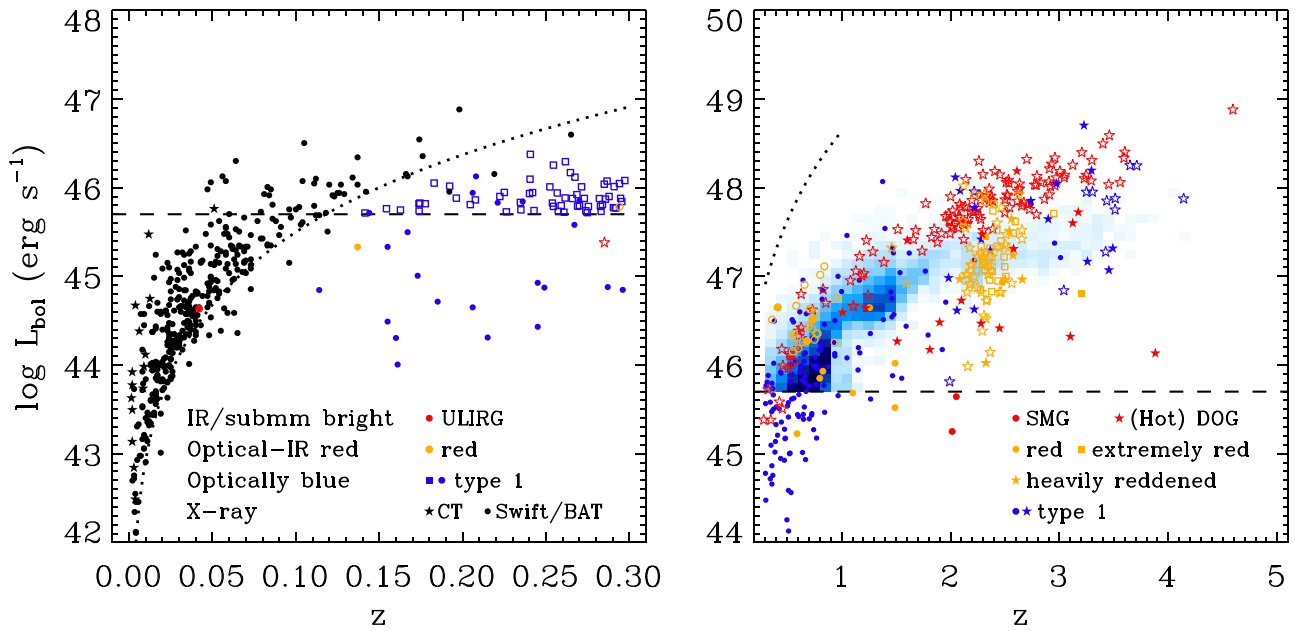


**Figure 2.** Bolometric luminosity ( $L_{\text{bol}}$ ) as a function of redshift (left:  $z < 0.3$ , right:  $z > 0.3$ ) for AGNs having  $f_{\text{Edd}}$  and measurements of either  $N_{\text{H}}$  (filled symbols) or  $E(B - V)$  (open symbols, plotted together if they have both  $N_{\text{H}}$  and  $E(B - V)_{\text{cont}}$ ). The samples plotted are ULIRGs/SMGs (A08, red circles), Hot DOGs (S14; A15; A16; R17a; V18a; Z18; A20, red stars), optical-IR red AGN samples named red quasars (U12; L16; L17; G17; K18, yellow circles), extremely red quasars (P19, yellow squares), heavily reddened quasars (B12; B13; B15a; T19; L20, yellow stars), Compton-thick AGNs (B15b; B16, black stars), Swift/BAT AGNs (R17c, black circles), and optically selected SDSS type 1 quasars (J13, blue squares for  $z < 0.3$ , density plot for  $z > 0.3$  (due to a large sample), matched with Y09 in blue circles; WISSH quasars from M17 and V18b as blue stars). The  $L_{\text{bol}} \geq 10^{45.7} \text{ erg s}^{-1}$  boundary is marked (dashed line), and a constant 14–195 keV flux of  $10^{-11} \text{ erg s}^{-1} \text{ cm}^{-2}$  with bolometric correction applied (Section 4) roughly denotes the detection limit of Swift/BAT X-ray data (dotted line, drawn up to  $z = 1$ ).

Hot DOGs (S14; A15<sup>8</sup>; A16; R17a; V18a; Z18; A20), and broad-line (AGN-like) SMGs (A08 with  $N_{\text{H}}$  from Alexander et al. 2005) were also included, adding part of some samples at  $z < 0.3$  that extend to  $z > 0.3$  (A08; Y09; J13; L16; R17c; K18).

Duplication among the samples was found in Compton-thick AGNs (B15b; B16), heavily reddened quasars (B12; T19), and red quasars (U12; K18), where we used the most recent values, except for those between B15b/B16 and R17c, where we kept both the  $N_{\text{H}}$  and  $f_{\text{Edd}}$  estimates as they were based on multiple X-ray observations. The samples based on follow-up studies of SDSS quasars were separated into those with  $N_{\text{H}}$  (Y09; M17) and those with  $E(B - V)$  (J13; V18b), where the  $f_{\text{Edd}}$  values from signal-to-noise ratio ( $S/N$ )  $> 20$  spectra in Shen et al. (2011) and Pâris et al. (2012) were added. We removed beamed sources (R17c, flagged by Koss et al. 2017 using the blazar catalog from Massaro et al. 2015) for reliable  $N_{\text{H}}$  and  $f_{\text{Edd}}$  values (but see also, e.g., Baek et al. 2019, for estimation of  $f_{\text{Edd}}$  in radio-bright AGNs). We used line widths corrected for instrumental resolution in estimating  $M_{\text{BH}}$  (Section 4).

### 3. Gas and Dust Obscuration

We compiled  $N_{\text{H}}$  and  $E(B - V)$  values, representing gas and dust obscuration, for the AGN samples. For  $N_{\text{H}}$ , we used the line-of-sight X-ray obscuration from sources with enough X-ray counts to model the spectra ( $\gtrsim 40$ – $60$ , defined by the respective references). Exceptions are obviously large absorption ( $N_{\text{H}} \geq 10^{24} \text{ cm}^{-2}$ ) constraints in S14, V18a, and A20, where the exposure times are longer than 20 ks but have a relatively smaller number of X-ray counts due to Compton-thick absorption. We add these values to our analysis. The

choice of models to fit or estimate the X-ray obscuration varies in the literature: Murphy & Yaqoob (2009) (S14; L16; G17; V18a; Z18), Brightman & Nandra (2011) (B15b; A16; B16; C16; A20), hardness-ratio-based  $N_{\text{H}}$  conversion (L17), (absorbed) power-law fit (Y09; C16; M17; G18; L20), and a combination of models (A08; R17c; T20). Still, when the  $N_{\text{H}}$  values are compared between various models (e.g., B15b; B16; G17; Z18; L20), they are mostly consistent within the uncertainties (but see also B15b and Liu & Li 2015 for the limitations of the models at Compton-thick column densities).

For  $E(B - V)$ , we used the UV/optical-IR continuum SED-based  $E(B - V)_{\text{cont}}$ <sup>9</sup> from the literature. Lower limits in  $E(B - V)$  were given to the P19 data from Hamann et al. (2017) because of likely underestimation using a narrow range of wavelengths to determine  $E(B - V)$ . For optical quasars, we determined the rest-frame  $> 0.3 \mu\text{m}$  power-law continuum slope  $\alpha$  following  $F_{\nu} \propto \nu^{\alpha}$ , fit to the photometric SED. We assumed an intrinsic slope of  $\alpha = 0.1 \pm 0.2$  from the most blue (hot dust-poor,  $\sim 3\sigma$  outliers) quasars in J13, consistent with accretion disk models and polarized observations of quasar SEDs ( $\alpha \approx 1/3$ , e.g., Shakura & Sunyaev 1973; Kishimoto et al. 2008). We limited the sample to quasars with at least three SDSS optical or UKIDSS near-IR (Lawrence et al. 2007) photometric detections at rest-frame  $0.3$ – $1 \mu\text{m}$  and rest-frame near-IR detections at up to at least  $2.3 \mu\text{m}$  to decompose the SED into the power-law continuum and dust emission (see J13 for details). We converted  $\alpha$  into  $E(B - V)$  by reddening the intrinsic slope using a Milky Way extinction curve at  $0.3$ – $1 \mu\text{m}$  to match the observed value of  $\alpha$ , while fixing  $E(B - V) = 0$  when

<sup>8</sup> This sample is being updated by P. R. M. Eisenhardt et al. (2020, in preparation), but we simply refer to the numbers from A15 at this time.

<sup>9</sup> Throughout,  $E(B - V)_{\text{cont/bl/nl}}$  are those derived from the continuum SED and broad/narrow-line ratios, respectively, and the  $E(B - V)_{\text{nl}}$  values are only mentioned as lower limits to  $E(B - V)_{\text{cont}}$ . We used the Milky Way extinction curve with total-to-selective extinction of 3.1 when transforming extinction to  $E(B - V)$ .



**Table 1**  
AGN Samples

Name	Sample	Selection	Obscuration	$z$	$\log L_{\text{bol}} (\text{erg s}^{-1})$	$N$
B15b; B16	Compton-thick	Hard X-ray	$N_{\text{H}}$	0.001–0.051	42.5–45.8	16
R17c	Swift/BAT	Hard X-ray	$N_{\text{H}}, E(B - V)_{\text{nl}}$	0.00–0.27	40.8–46.9	366
Y09; M17; V18b	Type 1	Optical	$N_{\text{H}}, E(B - V)_{\text{cont}}$	0.15–4.26	44.8–48.7	174
J13	Type 1	Optical	$E(B - V)_{\text{cont}}$	0.14–4.13	45.7–48.2	14,531
L16; L17; G17	Red	Optical–IR	$N_{\text{H}}, E(B - V)_{\text{cont}}$	0.14–2.48	45.2–46.9	12
U12; K18	Red	Optical–IR	$E(B - V)_{\text{cont}}$	0.29–0.96	45.8–47.1	23
G18	Extremely red	Optical–IR	$N_{\text{H}}$	2.32	47.5	1
P19	Extremely red	Optical–IR	$E(B - V)_{\text{cont}}$	2.24–2.95	46.7–47.8	28
L20	Heavily reddened	Optical–IR	$N_{\text{H}}$	2.09–2.66	45.7–46.9	7
B12; B13; B15a; T19	Heavily reddened	Optical–IR	$E(B - V)_{\text{cont}}$	1.46–2.66	46.0–48.6	51
C16; T20	DOG	Optical–IR	$N_{\text{H}}$	1.22–5.22	43.8–48.2	15
S14; A16; R17a; V18a; Z18; A20	Hot DOG	IR	$N_{\text{H}}$	1.01–4.60	46.2–48.1	9
A15	Hot DOG	IR	$E(B - V)_{\text{cont}}$	0.29–4.59	45.4–48.9	129
A08	ULIRG, SMG	IR/submm	$N_{\text{H}}$	0.04–2.05	44.6–45.6	3

**Notes.** AGN samples used in this work. We refer to each reference as having the objects with values or constraints on obscuration or accretion rate, while the original catalog paper is provided in the text (Section 2). Here,  $N$  denotes the number of objects for each set of references having obscuration and accretion rate information used in Section 5, so they could be smaller than the number of sources from the references. The subscripts “cont” and “nl” under  $E(B - V)$  values are derived using the continuum SED and narrow-line ratios, respectively. The abbreviated references are Brightman et al. (2015) (B15b); Brightman et al. (2016) (B16); Ricci et al. (2017c) (R17c); Young et al. (2009) (Y09); Martocchia et al. (2017) (M17); Vietri et al. (2018) (V18b); Jun & Im (2013) (J13); LaMassa et al. (2016, 2017) (L16, L17); Glikman et al. (2017b) (G17); Urrutia et al. (2012) (U12); Kim & Im (2018) (K18); Goulding et al. (2018) (G18); Perrotta et al. (2019) (P19); Lansbury et al. (2020) (L20); Banerji et al. (2012, 2013, 2015) (B12, B13, B15a); Temple et al. (2019) (T19); Corral et al. (2016) (C16); Toba et al. (2020) (T20); Stern et al. (2014) (S14); Assef et al. (2016) (A16); Ricci et al. (2017a) (R17a); Vito et al. (2018) (V18a); Zappacosta et al. (2018) (Z18); Assef et al. (2020) (A20); Assef et al. (2015) (A15); Alexander et al. (2008) (A08).

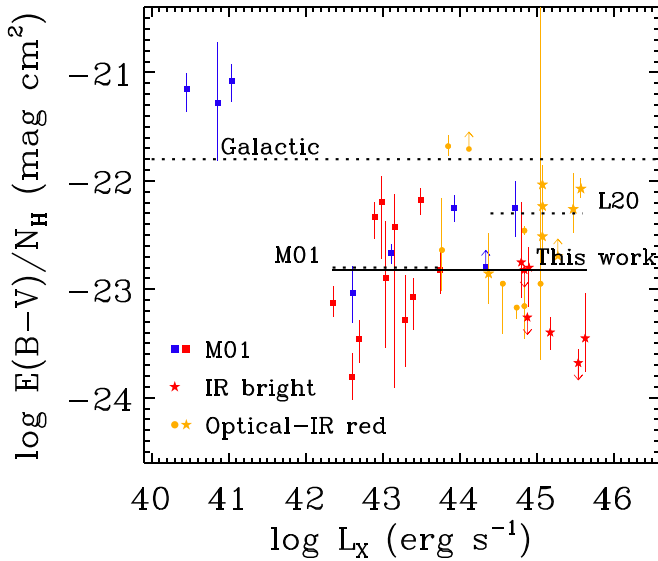


**Figure 3.** Log ratio between  $E(B - V)_{\text{cont/bl}}$  and  $N_{\text{H}}$ , plotted against intrinsic 2–10 keV luminosity. We plot only the data with  $N_{\text{H}}$  uncertainty values based on sufficient X-ray counts. The data come from Maiolino et al. (2001); marked M01, blue and red squares for type 1–1.5 and 1.8–2 classifications, respectively, red quasars (L16; G17; L17, yellow circles), heavily reddened quasars (L20, yellow stars), and Hot DOGs (S14; A16; R17a; Z18; A20, red stars). We show Galactic, L20, and Maiolino et al. (2001)  $\log E(B - V)/N_{\text{H}}$  values and the range of their applicable luminosities for obscured AGNs (dashed line), and likewise from this work (solid line).

$\alpha > 0.1$ . We checked if the  $E(B - V)$  estimates from J13 are consistent with the literature by comparing the values cross-matched with 17 sources in V18b and 277 sources in C. Carroll et al. (submitted) at  $E(B - V) < 0.5$  mag. The J13  $E(B - V)$  values have a median offset and scatter of  $0.05 \pm 0.05$  and  $0.04 \pm 0.06$  mag, respectively, consistent within the uncertainties. We adopt the J13 values for the cross-matched sources (Y09; M17; V18b).

The  $E(B - V)_{\text{cont}}$  values can suffer from host galaxy contamination in the rest-frame optical/near-IR. We limited the samples with the SEDs decomposed into an AGN and a host galaxy (U12; A15; L17) to  $L_{\text{bol}} \geq 10^{45.2} \text{ erg s}^{-1}$  for the decomposition to contain a sufficient AGN contribution, and the samples without an SED decomposition (the remaining samples with  $E(B - V)_{\text{cont}}$  in Table 1) to  $L_{\text{bol}} \geq 10^{45.7} \text{ erg s}^{-1}$ , to minimize host galaxy contamination. Above the luminosity limits, the average host contamination at 5100 Å drops below 50% and 10%, respectively, for type 1 quasars (Shen et al. 2011) and is consistent with the growing AGN contribution to the observed SEDs for red quasars at higher  $L_{\text{bol}}$  (L17). The  $L_{\text{bol}} \geq 10^{45.7} \text{ erg s}^{-1}$  limit corresponds to  $L_{\text{bol}} = 10^{12.1} L_{\odot}$ , selecting ULIRG luminosities for IR-bright AGNs (e.g., Fan et al. 2016; Toba et al. 2017). The majority of the hard X-ray selected AGNs from R17c are less luminous than the  $L_{\text{bol}}$  limits for  $E(B - V)_{\text{cont}}$ , but instead have robust measurements of  $N_{\text{H}}$  from their hard X-ray spectra.

The nuclear dust-to-gas ratio traced by the  $\log E(B - V)_{\text{cont/bl}}/N_{\text{H}}$  (mag cm<sup>2</sup>) values in Figure 3 is constant if the gas and dust obscuration are proportional (e.g., Usman et al. 2014). The values are overall smaller than the Galactic value (−21.8, e.g., Bohlin et al. 1978),<sup>10</sup> with reported average values ranging between −22.8 (Maiolino et al. 2001) and −22.3 (L20). L20 find relatively higher  $E(B - V)/N_{\text{H}}$  values for a sample of heavily reddened broad-line quasars at high luminosity, but there are similarly luminous quasars with relatively smaller  $E(B - V)/N_{\text{H}}$  values (i.e., the Hot DOGs or some optical–IR red quasars in Figure 3). Apart from the type 1 AGNs where the large scatter in  $E(B - V)/N_{\text{H}}$  could in part arise from the uncertainty constraining the lowest values in either quantity, we find the

<sup>10</sup> One of the reasons for the offset may be that the majority of the AGNs have an excess of dust-free gas within the sublimation radius (e.g., Risaliti et al. 2002, 2007; Maiolino et al. 2010; Burtcher et al. 2016; Ichikawa et al. 2019), but we focus here on the overall value when including the more luminous AGNs.

mean and scatter of  $\log E(B - V)/N_H(\text{mag cm}^2) = -22.77 \pm 0.51$  (observed) or  $\pm 0.41^{11}$  (intrinsic) from 31 obscured AGNs (type 2 AGNs, optical-IR red quasars, and Hot DOGs) without upper/lower limits in Figure 3, spanning absorption-corrected  $L_{2-10 \text{ keV}} = 10^{42.4-45.6} \text{ erg s}^{-1}$ . The ratios are close to the Maiolino et al. (2001) value, but are highly scattered for any combination of AGN type over the luminosity probed, complicating a simple correspondence between dust and gas. We thus refer to both  $E(B - V)$  and  $N_H$  when selecting AGNs with dusty gas, using a conversion of  $\log E(B - V)/N_H = -22.8$ .

The  $N_H$  and  $E(B - V)$  values are thought to be nuclear obscuration close to the AGN center, but as the AGN geometry consists of an extended, kpc order narrow-line region outside the central dusty structure (e.g., Kang & Woo 2018; Minezaki et al. 2019), we expect the narrow-line-based  $E(B - V)_{\text{nl}}$  values to be smaller than the  $E(B - V)_{\text{cont/bl}}$  values measured closer to the nucleus (e.g., Zakamska et al. 2003, 2005; Greene et al. 2014; Jun et al. 2020). For the R17c sample providing narrow Balmer decrements, we find that the  $E(B - V)_{\text{nl}}/N_H$  values for obscured (type 1.8–2.0) AGNs are about an order of magnitude smaller than the  $E(B - V)_{\text{cont}}/N_H$  values in Figure 3, although showing an even larger scatter. This demonstrates that  $E(B - V)_{\text{nl}}$  is simply much lower than  $E(B - V)_{\text{cont}}$ . Furthermore, the dust-to-gas ratios may decrease when using the global  $N_H$ , as it is larger than the nuclear line-of-sight  $N_H$ , such as for red quasars in L16, implying extended gas. The extended obscuration in obscured quasars will be considered to assess the effect of radiation pressure (Section 6.2), but for a better comparison of nuclear dust and gas obscuration, we remove  $E(B - V)_{\text{nl}}$  values from further analysis, and we use  $E(B - V)_{\text{cont}}$  as the fiducial estimate of  $E(B - V)$  hereafter.

#### 4. Eddington Ratio

Estimating  $f_{\text{Edd}}$  throughout the samples relies on several bolometric correction methods and black hole scaling relations. For the bolometric correction, we primarily relied on the hard X-ray (2–10 keV) luminosity to minimize the absorption correction for the X-ray samples in Table 1. The 2–10 keV intrinsic luminosities are based on a simple conversion of the 14–195 keV luminosities from R17c using a typical X-ray spectral slope; namely,  $L_{2-10 \text{ keV}} = 2.67 L_{14-195 \text{ keV}}$  (Rigby et al. 2009). The absorption-corrected X-ray-to-bolometric correction depends on  $L_{\text{bol}}$  or  $f_{\text{Edd}}$  (e.g., Marconi et al. 2004; Vasudevan & Fabian 2007; Lusso et al. 2012). We used the Marconi et al. (2004) bolometric correction as a function of  $L_{\text{bol}}$ , as the dynamic range of  $L_{\text{bol}}$  ( $\sim 3$ –4 dex) is wider than that of  $f_{\text{Edd}}$  ( $\sim 2$  dex). When the X-ray luminosity was absent, we adopted the monochromatic bolometric correction from IR or extinction-corrected UV/optical continuum or line luminosities, which are relatively insensitive to  $L_{\text{bol}}$  (e.g., Richards et al. 2006; Lusso et al. 2012). We used the corrections from  $L_{1350}$ ,  $L_{3000}$ , and  $L_{5100}^{12}$  (3.81, 5.15, and 9.26, respectively, Shen et al. 2011) for optical quasars (J13; V18b) and obscured AGNs with

extinction-corrected continuum luminosities (B12; B13; A15; B15a; objects in L17 without  $N_H$ ; T19; A20),  $L_{\text{P}\beta}$  ( $\log L_{\text{bol}}/10^{44} \text{ erg s}^{-1} = 1.29 + 0.969 \log L_{\text{P}\beta}/10^{42} \text{ erg s}^{-1}$ , Kim et al. 2015) for K18,  $L_{3.4\mu\text{m}}$  (8, Hamann et al. 2017) for P19,  $L_{15\mu\text{m}}$  (9, Richards et al. 2006) for U12, with each correction having systematic uncertainties of a few tens of percent up to a factor of a few (e.g., Heckman et al. 2004; Richards et al. 2006; Lusso et al. 2012).

We estimated  $M_{\text{BH}}$  mostly through stellar absorption or broad emission lines, using a mutually consistent methodology. The mass constant of single-epoch estimators for AGNs ( $f$ -factor), is determined assuming that the reverberation-mapped AGNs lie on the  $M_{\text{BH}}-\sigma_*$  relation for inactive galaxies. We thus use the same  $M_{\text{BH}}-\sigma_*$  relation (e.g., Woo et al. 2015),

$$\log\left(\frac{M_{\text{BH}}}{M_{\odot}}\right) = (8.34 \pm 0.05) + (5.04 \pm 0.28) \log\left(\frac{\sigma_*}{200 \text{ km s}^{-1}}\right), \quad (2)$$

to estimate  $\sigma_*$ -based  $M_{\text{BH}}$  values for narrow-line AGNs where the host absorption lines are better seen, and to derive the  $f$ -factor in the broad FWHM-based single-epoch  $M_{\text{BH}}$  estimators for broad-line AGNs where AGN emission dominates over the host galaxy. The  $M_{\text{BH}}(\sigma_*)$  estimates based on other  $M_{\text{BH}}-\sigma_*$  relations with a shallower slope, e.g., Kormendy & Ho (2013), are systematically offset to Equation (2) by 0.35 and  $-0.05$  dex at  $\sigma_* = 100$  and  $400 \text{ km s}^{-1}$ , respectively.

The single-epoch  $M_{\text{BH}}(L, \text{FWHM})$  estimators were empirically calibrated between  $H\beta$  and  $H\alpha$ ,  $\text{Mg II}$ , or  $\text{C IV}$  (Jun et al. 2015 using the Bentz et al. 2013  $R_{\text{BLR}}-L$  relation) with  $\text{C IV}$  blueshift correction when broad-line shifts were available (Jun et al. 2017), or were calibrated between hydrogen Balmer and Paschen series (Kim et al. 2010,<sup>13</sup> using the Bentz et al. 2009  $R_{\text{BLR}}-L$  relation), over a wide range of redshift and luminosity. This approach reduces the systematic offset from the choice of emission line by up to an order of magnitude<sup>14</sup> at extreme  $M_{\text{BH}}$  values (Jun et al. 2015), or at extreme  $\text{C IV}$  blueshifts (Jun et al. 2017). The estimators were updated using a common  $f$ -factor and uncertainty of  $1.12 \pm 0.31$  for the FWHM-based  $M_{\text{BH}}$  (Woo et al. 2015), as shown below:

$$\log\left(\frac{M_{\text{BH}}}{M_{\odot}}\right) = a + \log\left(\frac{f}{1.12}\right) + b \log\left(\frac{L}{10^{44} \text{ erg s}^{-1}}\right) + c \log\left(\frac{\text{FWHM}}{10^3 \text{ km s}^{-1}}\right) + d \log\left(\frac{\Delta v_{\text{C IV}}}{10^3 \text{ km s}^{-1}}\right). \quad (3)$$

<sup>13</sup> Using our adopted cosmology, we find that the  $R_{\text{BLR}}$  values from Bentz et al. (2013) are higher than from Bentz et al. (2009) by 0.00–0.03 dex for the luminosity range used to derive Paschen line  $M_{\text{BH}}$  values ( $L_{5100} = 10^{43.5-46} \text{ erg s}^{-1}$ , A08; K18). K18 also note that using a single Gaussian to fit the broad Paschen lines will underestimate the  $M_{\text{BH}}$  values by 0.06–0.07 dex, but these amounts are negligible compared to the significance of the results (Section 5).

<sup>14</sup> We note that a nonlinear relation between  $\sigma$  and FWHM values could further result in positive/negative biases in the FWHM-based  $M_{\text{BH}}$  estimate at notably high and low FWHM values (e.g., Peterson et al. 2004; Collin et al. 2006), as well as whether to construct the UV or IR mass estimators to match the  $M_{\text{BH}}$  values to the Balmer line based, or to match the UV or IR broad-line widths and the luminosities to the optical values separately. Our choice of  $M_{\text{BH}}$  estimators has its own merits and limitations, and we test the systematic uncertainty of  $M_{\text{BH}}$  in Section 5.

<sup>11</sup> We refer to the intrinsic scatter of the quantity  $x = \log E(B - V)/N_H$ ,  $\sigma_{\text{int}}$ , as the observed scatter with measurement error  $\Delta x$  subtracted in quadrature, that is,  $\sigma_{\text{int}}^2 = \sigma_{\text{int}}^2 \{ (x_i + 22.77)^2 - \Delta x_i^2 \} / (n - 1)$ . The errors on  $E(B - V)$  values are missing for the L16 and G17 samples, but the intrinsic scatter of  $\log E(B - V)/N_H$  decreases by only 0.01 dex if we assign the mean error of  $\Delta E(B - V) = 0.12 \text{ mag}$  from the L17 sample used here.

<sup>12</sup> Throughout, subscripts of  $L$  indicate monochromatic continuum luminosity at that wavelength, measured in units of Å.

**Table 2**  
AGN  $M_{\text{BH}}$  Estimators

Type	$a$	$b$	$c$	$d$
$M_{\text{BH}}(L_{1350}, \text{FWHM}_{\text{C IV}})$	$6.99 \pm 0.16$	$0.547 \pm 0.037$	$2.11 \pm 0.11$	0
$M_{\text{BH}}(L_{1350}, \text{FWHM}_{\text{C IV}}, \Delta v_{\text{C IV}})$	$6.62 \pm 0.16$	$0.547 \pm 0.037$	$2.11 \pm 0.11$	$0.335 \pm 0.022$
$M_{\text{BH}}(L_{3000}, \text{FWHM}_{\text{Mg II}})$	$6.57 \pm 0.13$	$0.548 \pm 0.035$	$2.45 \pm 0.06$	0
$M_{\text{BH}}(L_{5100}, \text{FWHM}_{\text{H}\beta})$	$6.88 \pm 0.12$	$0.533 \pm 0.034$	2	0
$M_{\text{BH}}(L_{5100}, \text{FWHM}_{\text{H}\alpha})$	$6.99 \pm 0.12$	$0.533 \pm 0.034$	$2.12 \pm 0.03$	0
$M_{\text{BH}}(L_{\text{P}\beta}, \text{FWHM}_{\text{P}\beta})$	$7.24 \pm 0.16$	$0.45 \pm 0.03$	$1.69 \pm 0.16$	0
$M_{\text{BH}}(L_{\text{P}\alpha}, \text{FWHM}_{\text{P}\alpha})$	$7.20 \pm 0.16$	$0.43 \pm 0.03$	$1.92 \pm 0.18$	0

**Notes.**  $L$  is the continuum or broad-line luminosity, FWHM is the full width at half maximum of the best-fit broad-line model, and  $\Delta v_{\text{C IV}}$  is the broad C IV line offset to the systemic redshift (Shen et al. 2011 in J13, negative for blueshifts).  $a$ ,  $b$ ,  $c$ ,  $d$  are the coefficients in Equation (3).

The set of  $(a, b, c, d)$  values for the combination of  $M_{\text{BH}}(L, \text{FWHM}, \Delta v)$  are given in Table 2. For broad-line AGNs with X-ray observations and single-epoch UV/optical  $M_{\text{BH}}$  estimates, we converted the X-ray-based  $L_{\text{bol}}$  into  $L_{1350}$ ,  $L_{3000}$ ,  $L_{5100}$  using the aforementioned bolometric corrections, to minimize host galaxy contamination in 1350–5100 Å. We removed sources with Balmer line widths similar to [O III] (A08) to distinguish broad lines from broadening by ionized gas outflows. We also limited the FWHM values to  $\leq 10,000 \text{ km s}^{-1}$  where values otherwise (e.g., 4% of the J13 sample) are potentially affected by rotating accretion disks and show double-peaked lines (e.g., Chen & Halpern 1989; Eracleous & Halpern 1994; Table 4 in Jun et al. 2017). Meanwhile, R17c removed single-epoch  $M_{\text{BH}}$  estimates for  $N_{\text{H}} \geq 10^{22} \text{ cm}^{-2}$  AGNs as the emission line profiles could be modified by obscuration or are dominated by the narrow component (Koss et al. 2017). However, as we already removed type  $\geq 1.8$  sources when estimating  $M_{\text{BH}}$  for broad-line AGNs, we keep the  $N_{\text{H}} \geq 10^{22} \text{ cm}^{-2}$  sources. These obscured type  $\leq 1.5$  AGNs with  $M_{\text{BH}}(\text{FWHM})$  in R17c do not significantly change the distribution of  $N_{\text{H}}-f_{\text{Edd}}$  with respect to using  $M_{\text{BH}}(\sigma_*)$  values. This hints that obscuration does not significantly bias the single-epoch  $M_{\text{BH}}$  estimates for broad-line AGNs, also consistent with the independence of broad C IV-to-H $\beta$  line width ratios with respect to the continuum slope for type 1 quasars (e.g., Jun et al. 2017). We thus carefully selected only the type  $\leq 1.5$  sources when using rest-frame UV–optical spectra to estimate  $M_{\text{BH}}(\text{FWHM})$  for AGNs.

Among single-epoch  $M_{\text{BH}}$  estimates with multiple broad-line detections, we adopted the estimators in the order of decreasing rest wavelength, while direct dynamical (B15b; B16; R17c) or reverberation-mapped (Bentz & Katz 2015 in R17c)  $M_{\text{BH}}$  values were adopted over other methods. Hot DOGs, which are heavily obscured AGNs typically showing strong, narrow lines, often display signatures of narrow-line outflows instead of ordinary broad emission lines (e.g., Wu et al. 2018; Jun et al. 2020). Unless the sources are thought to show scattered or leaked light from the broad-line region (A16; A20), we utilized the SED fit from A15 when deriving the  $M_{\text{BH}}$  constraints. Applying their maximal stellar mass ( $M_*$ ) estimates from the SED fit, we gave upper limits to the  $M_{\text{BH}}$  values using the  $M_{\text{BH}}-M_*$  relation. The  $M_{\text{BH}}/M_*$  values are thought to evolve less with redshift ( $\propto (1+z)^\gamma$ ,  $\gamma \lesssim 1$ ) than  $M_{\text{BH}}/M_{\text{bulge}}$  (e.g., Bennert et al. 2011; Ding et al. 2020; Suh et al. 2020). We adopt  $M_{\text{BH}}/M_* \sim 0.003$  from the  $z \sim 1$ –2 AGNs in

Ding et al. (2020) and Suh et al. (2020). The same relation was used to estimate  $M_{\text{BH}}$  for the DOGs in C16 and T20.

Although this analysis attempted to consistently estimate  $M_{\text{BH}}$  for the various samples, systematic uncertainties of a factor of several are expected from the intrinsic scatter in the BH–host mass scaling relations (e.g., Kormendy & Ho 2013) and the  $R_{\text{BLR}}-L$  relation (e.g., Bentz et al. 2013; Du et al. 2014). Overall, the compiled  $L_{\text{bol}}$  and  $M_{\text{BH}}$  estimates each have systematic uncertainties of up to a factor of several or more, and although the AGN  $M_{\text{BH}}$  estimators include the  $\sim L^{0.5}$  dependence, reducing uncertainty from the bolometric correction going into  $f_{\text{Edd}} \propto L_{\text{bol}}/M_{\text{BH}}$ , we still expect systematic uncertainties of a factor of several in  $f_{\text{Edd}}$ . We thus will interpret only the group behavior of each AGN sample within the uncertainties in  $f_{\text{Edd}}$ .

## 5. Results

In Figure 4 we plot the distributions of  $N_{\text{H}}-f_{\text{Edd}}$  and  $E(B-V)-f_{\text{Edd}}$  for the collection of AGN samples. It is clear that the forbidden region for dusty gas (Figure 1), previously less occupied by the AGNs from R17c, is well populated with IR/submillimeter-selected and optical–IR red quasars, with a minor fraction of type 1 quasars. This is seen in both the  $N_{\text{H}}-f_{\text{Edd}}$  and the  $E(B-V)-f_{\text{Edd}}$  diagrams. We investigate this further in Figure 5, where we show the fraction of sources in the forbidden zone (i.e.,  $N_{\text{H}} \geq 10^{22} \text{ cm}^{-2}$ ,  $f_{\text{Edd,dust}} > 1$ ) per bolometric luminosity bin as a function of  $L_{\text{bol}}$ . In the following, this fraction is referred to as  $\varphi$ . It is clear that  $\varphi$  is minimal among the X-ray-selected AGNs with  $\varphi_{N_{\text{H}}} \lesssim 10\%$  at  $L_{\text{bol}} \sim 10^{42-47} \text{ erg s}^{-1}$ . Similarly, optically selected quasars have  $\varphi_{N_{\text{H}}}$  and  $\varphi_{E(B-V)} \lesssim 20\%$  at  $L_{\text{bol}} \sim 10^{44-48} \text{ erg s}^{-1}$ , with some uncertainty for  $\varphi_{N_{\text{H}}}$  at  $L_{\text{bol}} \sim 10^{47-48} \text{ erg s}^{-1}$ . In contrast, the optical–IR red and IR/submillimeter-bright quasars (hereafter referred to together as luminous, obscured quasars) commonly lie mostly in the forbidden region over a wide range of  $N_{\text{H}}$  and  $E(B-V)$  values, and we combined their statistics.<sup>15</sup> The luminous, obscured quasars show  $\varphi_{N_{\text{H}}}$  and  $\varphi_{E(B-V)} \gtrsim 60\%$  at  $L_{\text{bol}} \sim 10^{46-48} \text{ erg s}^{-1}$ , significantly higher than the less-luminous X-ray AGNs at comparable obscuration, or the comparably luminous but less obscured optical quasars. These findings confirm earlier studies by Glikman (2017a)

<sup>15</sup> A potential caveat is the difference in the dust-to-gas ratio observed between optical–IR red and IR/submillimeter-bright quasars, which may bias the  $\varphi$  value between the populations. The average dust-to-gas ratios for each population from Section 3 are  $\langle \log E(B-V)/N_{\text{H}} \rangle = -22.33$  and  $-22.88$ , respectively. Using the separate ratios, however,  $\varphi_{E(B-V)}$  (Figure 5 right) still remains consistent between the two populations.



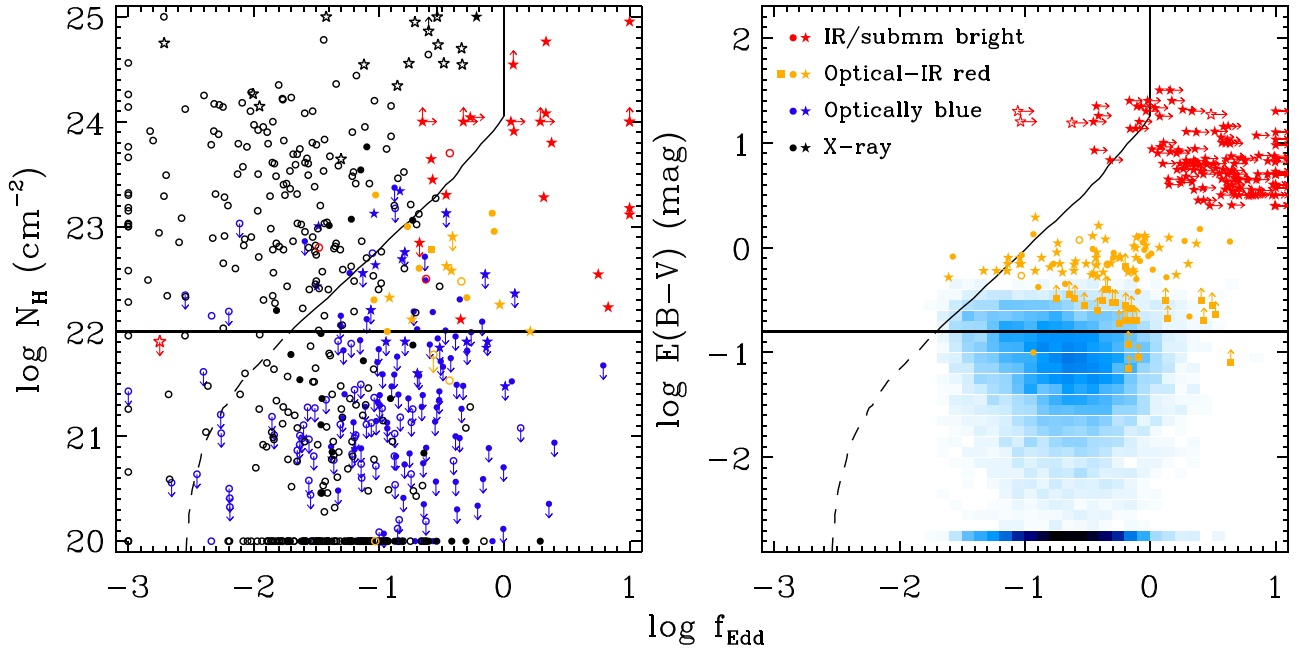


**Figure 4.** The  $N_{\text{H}}-f_{\text{Edd}}$  plane showing AGNs selected at different wavelengths. Horizontal lines separate obscured/unobscured AGNs at  $N_{\text{H}} = 10^{22} \text{ cm}^{-2}$ , and the effective Eddington ratio curves are plotted as solid/dashed lines with respect to  $N_{\text{H}} = 10^{22} \text{ cm}^{-2}$ . The symbols and color format follow that of Figure 2, except that the symbols are now filled when  $L_{\text{bol}} \geq 10^{45.7} \text{ erg s}^{-1}$  and open otherwise. Data outside the plotted region are shown along the boundary.

and L20 on optical–IR red quasars, with our results applicable to general luminous, obscured quasars.

Systematic uncertainties of a factor of several in  $f_{\text{Edd}}$  (Section 4) may change the fraction of the samples in the forbidden region. We test this by giving a  $\pm 0.5$  dex offset to the  $f_{\text{Edd,dust}}(N_{\text{H}}) = 1$  curve and recalculating  $\varphi$ . The  $\varphi$  values are nearly unchanged for the X-ray AGNs and optical quasars, whereas for the luminous, obscured quasars,  $\varphi$  may drop down to 40%–50% at  $L_{\text{bol}} \sim 10^{46-48} \text{ erg s}^{-1}$  if the observed  $f_{\text{Edd}}$  values are overestimated by 0.5 dex. Still, the  $\varphi$  values for the luminous, obscured quasars are several times the X-ray AGNs or optical quasars at a given luminosity, and the main trend in Figure 5 remains unchanged. Modifications to the  $f_{\text{Edd,dust}}$  curve may also occur when considering the effect of dust-to-gas ratios closer to the Milky Way value than the value adopted in this work, or radiation trapping. The enhanced absorption of the incident radiation by dust or trapping of reprocessed radiation lowers the  $f_{\text{Edd,dust}}$  curve, at  $N_{\text{H}} \geq 10^{22} \text{ cm}^{-2}$  (Ishibashi et al. 2018). Still, we note that both effects simply increase  $\varphi$  for luminous, obscured quasars, reinforcing our findings in Figures 4 and 5.

The  $f_{\text{Edd,dust}}$  values can be further shifted by nuclear stars. Adopting the sphere of influence from the BH, we have

$$r_{\text{BH}} = GM_{\text{BH}}/\sigma_*^2 = 107 \text{ pc} \left( \frac{M_{\text{BH}}}{10^9 M_{\odot}} \right) \left( \frac{\sigma_*}{200 \text{ km s}^{-1}} \right)^{-2}, \quad (4)$$

and the enclosed mass  $M(<r)$  becomes multiple times larger than  $M_{\text{BH}}$  at  $r \gtrsim r_{\text{BH}}$  due to nuclear stars, increasing the  $L_{\text{Edd,dust}}$  in Equation (1) for a radiation pressure force to balance off a stronger gravity by  $M(<r)/M_{\text{BH}}$  times. Nuclear stars may lower  $f_{\text{Edd,dust}}$  significantly if the BH is undermassive relative to the  $M_{\text{BH}}-M_*$  relation, or if the stellar light is more concentrated near the center. To fully explain the excess  $\varphi$  in luminous, obscured quasars by the shift in  $L_{\text{Edd,dust}}$  values,

however, their negative offset on the  $M_{\text{BH}}-M_*$  relation should be on average an order of magnitude, which is less likely from current observations (e.g., Bongiorno et al. 2014, but see also U12, where a fraction of their sample show undermassive  $M_{\text{BH}}/M_*$  values). Instead, assuming  $M_{\text{BH}}/M_* \sim 0.003$  from  $z \sim 1-2$  AGNs (Ding et al. 2020; Suh et al. 2020), we find that the Sérsic index (Sérsic 1963) for luminous, obscured quasars should still be  $\approx 2.5-3$  times larger than for the typical AGN for  $M(<r_{\text{BH}})/M_{\text{BH}}$  to be boosted by an order of magnitude, which is likewise a stringent condition. Therefore, we find that nuclear stars themselves are less likely to shift  $f_{\text{Edd,dust}}$  values enough to falsify our results.

We note that the IR-luminous, obscured quasars appear to show higher  $\varphi_{N_{\text{H}}}$  values compared to obscured (type 1.8–2), X-ray-selected quasars at matched luminosity. The type 1.8–2 sources in R17c have  $\varphi_{N_{\text{H}}}$  values  $\lesssim 20\%$ , still avoiding the forbidden region by factors of several compared to the IR-luminous, obscured quasars at  $L_{\text{bol}} \gtrsim 10^{46} \text{ erg s}^{-1}$ . We caution that the IR-luminous, obscured quasars are intrinsically different from the obscured, BAT-selected quasars, however, as the Swift/BAT survey is missing the distant, obscured quasar population often detected by deeper X-ray observations (e.g., Merloni et al. 2014; see the references in Table 1).

## 6. Discussion

The luminous, obscured quasars are known to be a substantial population in the intermediate-redshift universe, as their combined number density is comparable to that of unobscured quasars at matched luminosity (A15; B15a; Hamann et al. 2017; Glikman et al. 2018). As the typical  $M_{\text{BH}}$  values for  $L_{\text{bol}} > 10^{46} \text{ erg s}^{-1}$  quasars in this work are similar ( $\sim 10^9 M_{\odot}$ ) for both the obscured and unobscured populations, the timescale of the luminous, obscured quasar phase with  $f_{\text{Edd,dust}} > 1$  is presumed to be similar to that of the  $f_{\text{Edd,dust}} < 1$  quasars. In contrast, the nearly complete absence

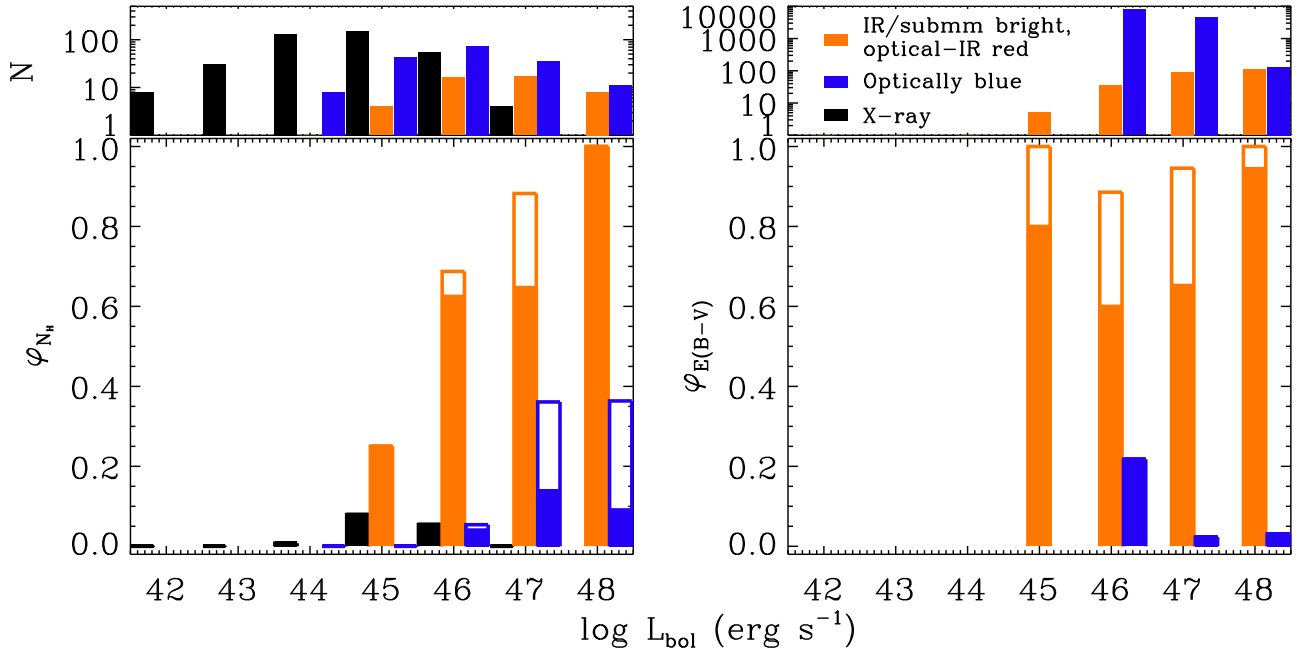


**Figure 5.** Fraction of AGNs in the forbidden region ( $\phi$ ) on the  $N_H$ - $f_{\text{Edd}}$  (bottom left) and  $E(B - V)$ - $f_{\text{Edd}}$  (bottom right) planes, with the number of sources used to plot the fractions in each luminosity bin (top). The solid graphs indicate the minimum value of  $\phi$  for the given upper and lower limits on obscuration or  $f_{\text{Edd}}$ , whereas the open graphs include all of the upper and lower limits enclosing the forbidden region. The colors for X-ray and optically blue AGNs follow those of Figures 2 and 4, whereas we merge the optical-IR red and IR/submillimeter-bright samples that show similar  $\phi$  values, in orange. The graphs are plotted when the number of AGNs  $\geq 4$  per bin, offset to each other only for display purposes, and are calculated based on a common interval in  $L_{\text{bol}}$ .

of lower-luminosity AGNs with  $f_{\text{Edd,dust}} > 1$  (Section 5) suggests a much shorter obscured phase for lower-luminosity AGNs. This appears as a challenge for the radiation-pressure feedback in regulating the nuclear obscuration for luminous quasars, and we next consider possible evolutionary scenarios to achieve a coherent picture of dust obscuration in luminous quasars.

### 6.1. Active Timescale

First, the AGN timescale (hereafter  $t_{\text{AGN}}$ ) is thought to be shorter for more luminous quasars, and this may explain higher  $\phi$  values for luminous quasars. The nearby AGN fraction is measured to be tens of percent of the galaxy lifetime (e.g., Ho et al. 1997; Kauffmann et al. 2003), with a corresponding  $t_{\text{AGN}}$  of  $\sim 10^9$  yr assuming typical galaxy lifetimes of  $\sim 10^{10}$  yr. More luminous quasars are more rare, with expected  $t_{\text{QSO}} \sim 10^{7-8}$  yr (e.g., Martini 2004; Hopkins et al. 2005; Hopkins & Hernquist 2009). To explain  $\phi \lesssim 1\%$ – $10\%$  for  $L_{\text{bol}} \lesssim 10^{44}$  erg s $^{-1}$  AGNs in Figure 5, we constrain the timescale for radiation pressure to clear the nuclear obscuration (hereafter the radiation feedback timescale,  $t_{\text{rad}} = t_{\text{AGN}} \phi$ ) to be  $t_{\text{rad}} \lesssim 10^9 (0.01\text{--}0.1) \sim 10^{7-8}$  yr. Assuming that luminous, obscured quasars will evolve into comparably luminous unobscured quasars through radiation-pressure feedback, so as to explain the comparable number density between the populations,  $t_{\text{rad}}$  for luminous ( $L_{\text{bol}} \gtrsim 10^{46}$  erg s $^{-1}$ ) quasars with  $\phi \gtrsim 60\%$  would be  $t_{\text{rad}} \sim 0.5 t_{\text{QSO}} \phi \sim 0.5 (10^{7-8}) (0.6 - 1) = (3 - 5) \times 10^{6-7}$  yr, roughly comparable to  $t_{\text{rad}}$  for less-luminous AGNs. We note that if AGN activity is more episodic (e.g., Park & Ricotti 2011; Yajima et al. 2017), feedback timescales may be shortened accordingly, although it seems more likely that luminous quasars have few episodes of vigorous accretion (e.g., Hopkins & Hernquist 2009). Luminous, obscured quasars may thus appear to show higher  $\phi$  values due to a shorter  $t_{\text{AGN}}$  than less-luminous, obscured AGNs, even if they feel the same radiation pressure.

We have referred to  $t_{\text{QSO}} \lesssim 10^{7-8}$  yr for quasars as a whole (e.g.,  $M_B \lesssim -23$  mag or  $L_{\text{bol}} \gtrsim 10^{45}$  erg s $^{-1}$ ), but if more luminous, obscured quasars are in a shorter phase of AGN evolution (shorter  $t_{\text{AGN}}$ ), it better explains the highest  $\phi$  values observed at  $L_{\text{bol}} \gtrsim 10^{46}$  erg s $^{-1}$ . L20 note outflow timescales ( $t_{\text{out}}$ ) for nuclear obscuration to clear away in an expanding shell by radiation pressure on dust,

$$t_{\text{out}} \approx 2 \times 10^5 \text{ yr} \left( \frac{r_0}{30 \text{ pc}} \right) \left( \frac{v_{\text{out}}}{1000 \text{ km s}^{-1}} \right)^{-1}, \quad (5)$$

finding  $t_{\text{out}} \approx 2 \times 10^5$  yr for Compton-thick gas expanding from an initial distance of  $r_0 = 30$  pc until it reaches  $N_H = 10^{22}$  cm $^{-2}$ , assuming  $v_{\text{out}} = 10^3$  km s $^{-1}$ . If the dusty gas outflows are triggered by radiation pressure, we expect  $t_{\text{out}}$  to be equal to  $t_{\text{rad}}$ . However, it is shorter than our estimated  $t_{\text{rad}}$  values for luminous quasars, by  $\sim \{(3 - 5) \times 10^{6-7}\} / (2 \times 10^5)$  or  $\sim 1$ – $2$  orders of magnitude. This can be explained if  $t_{\text{AGN}}$  for  $L_{\text{bol}} \gtrsim 10^{46}$  erg s $^{-1}$  quasars are  $\sim 1$ – $2$  orders of magnitude shorter than the  $t_{\text{QSO}} \sim 10^{7-8}$  yr we adopt, qualitatively consistent with the drop of  $t_{\text{AGN}}$  for more luminous quasars in simulations (e.g., Hopkins et al. 2005, 2006).

### 6.2. Extended Obscuration

An alternative description is that it takes a longer  $t_{\text{rad}}$  for luminous, obscured quasars to clear their obscuration than at lower luminosity. Radiation pressure from luminous, obscured quasars should effectively reach larger distances in the galaxy according to the decreasing small-scale dust covering factor observed in high  $L_{\text{bol}}$  or  $f_{\text{Edd}}$  AGNs (e.g., Maiolino et al. 2007; Toba et al. 2014; Ezhikode et al. 2017). Thus, observing high  $\phi$  values in luminous, obscured quasars implies that dusty gas may be spatially extended into their hosts, in contrast to lower-luminosity AGNs. This is supported by observations of



obscured quasars showing an extended distribution of disturbed emission (e.g., Sanders et al. 1988; Sanders & Mirabel 1996; Urrutia et al. 2008; Glikman et al. 2015; Fan et al. 2016; Ricci et al. 2017b). An increased fraction of obscured yet broad-line AGNs (e.g., Lacy et al. 2015; Glikman et al. 2018) or extended dust extinction through lines of sight kiloparsecs away from narrow-line AGNs are seen (Section 3) at quasar luminosities, also in agreement with global column densities much larger than the line-of-sight  $N_H$  for red quasars (Section 3).

According to simplified models for AGNs and host galaxy obscuration at multiple scales (e.g., Buchner & Bauer 2017; Hickox & Alexander 2018), the host galaxy kiloparsecs away from the nucleus is responsible for  $N_H \sim 10^{22} \text{ cm}^{-2}$ , whereas obscuration from the inner AGN structure ( $\lesssim 10 \text{ pc}$ ) or circum-nuclear starbursts ( $\sim 10\text{--}100 \text{ pc}$ ) can reach Compton-thick column densities. In addition, obscuration from gas-rich mergers (e.g., Hopkins et al. 2008) or higher gas fractions in high-redshift galaxies (e.g., Tacconi et al. 2010; Buchner & Bauer 2017) may enhance the obscuration up to kiloparsec scales. Coming back to Equation (5), we find that  $t_{\text{out}}$  for luminous, obscured quasars will be extended by 1–2 orders of magnitude ( $t_{\text{out}} \sim 10^{6-7} \text{ yr}$ ) if extended obscuration due to mergers is spread over  $\sim 10^{2-3} \text{ pc}$ , closing the gap between the timescale arguments (Section 6.1) without even changing  $t_{\text{AGN}}$ . This scenario is also consistent with the  $t_{\text{out}}$  values estimated by modeling expanding shells of dusty gas located  $\sim 10^{2-3} \text{ pc}$  away from luminous quasars (Ishibashi et al. 2017). We direct readers to the theoretical and observational studies on how the nuclear outflows triggered by radiation pressure extend to the host galaxy (e.g., Harrison et al. 2014; Ishibashi & Fabian 2015; Thompson et al. 2015; Ishibashi et al. 2017; Kang & Woo 2018).

Although the impact of radiation pressure from the AGN itself is weaker at extended regions of the galaxy, and R17c separate radiation-pressure feedback from inflows and outflows, radiation pressure has still been considered to launch outflows that may reach large distances (e.g., Hopkins & Elvis 2010 and the discussion in L20). In this work, we separately considered radiation pressure to regulate  $\lesssim 10 \text{ pc}$  order obscuration and outflows on  $\sim 10^{2-3} \text{ pc}$  scales, but we note that radiation pressure is thought to cause extended outflows that eventually clear obscured quasars, according to gas-rich, merger-driven quasar evolution models (e.g., Hopkins et al. 2008; Hickox et al. 2009). Not only are the highly ionized gas outflows on the order of  $\sim 10^3 \text{ km s}^{-1}$  found in the majority of quasars with  $L_{\text{O III}} \gtrsim 10^{42} \text{ erg s}^{-1}$  (or  $L_{\text{bol}} \gtrsim 10^{45.5} \text{ erg s}^{-1}$ ), or  $f_{\text{Edd}} \gtrsim 0.1$  (e.g., Woo et al. 2016; Rakshit & Woo 2018; Shin et al. 2019; Jun et al. 2020), they extend over kiloparsec scales together with Balmer line outflows with a weaker ionization potential or molecular outflows (e.g., Fiore et al. 2017; Kang et al. 2017; Fluetsch et al. 2019). This is in line with higher merger fractions seen in  $L_{\text{bol}} \gtrsim 10^{46} \text{ erg s}^{-1}$  quasars (e.g., Treister et al. 2012; Fan et al. 2016; Díaz-Santos et al. 2018), which is also the transitional luminosity where radiation-pressure feedback appears less effective (Figure 5).

We thus consider radiation pressure to be responsible for regulating not only the  $\lesssim 10 \text{ pc}$  order dusty structure (e.g., Lawrence 1991; R17c), but also the host galaxy environment in obscured  $L_{\text{bol}} \gtrsim 10^{46} \text{ erg s}^{-1}$  quasars where the triggered nuclear outflows may reach and clear  $\sim 10^{2-3} \text{ pc}$  scale material, slowly over a timescale of  $\sim 10^{6-7} \text{ yr}$ . This is consistent with the high- $f_{\text{Edd}}$  AGN outflows discussed in R17c, though their sample lacked the luminous quasars that we argue are responsible for

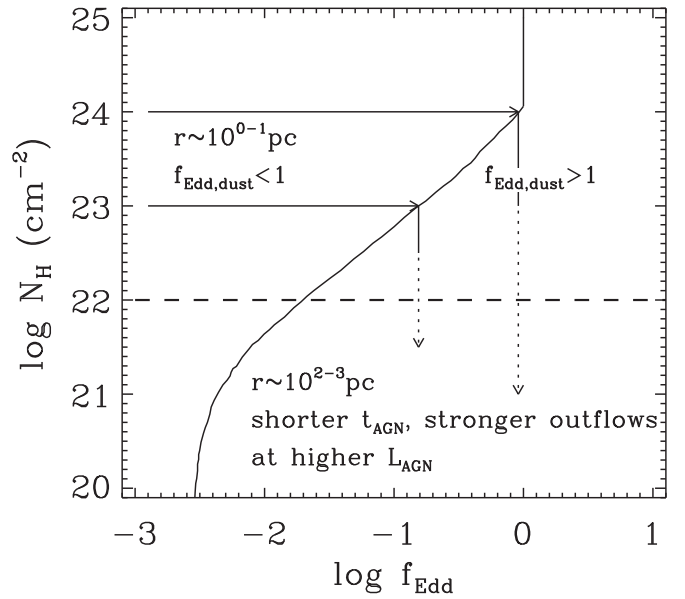


**Figure 6.** Schematic diagram showing the maximally allowed accretion rate and radiation-pressure/outflow track on the  $N_H$ - $f_{\text{Edd}}$  plane for  $N_H = 10^{23}, 10^{24} \text{ cm}^{-2}$  quasars. At  $L_{\text{bol}} \lesssim 10^{45} \text{ erg s}^{-1}$ , the lack of objects in the forbidden region suggests that radiation pressure on dusty gas controls nuclear ( $\lesssim 10 \text{ pc}$  order) obscuration and quickly drops the obscuration down to  $N_H \lesssim 10^{22} \text{ cm}^{-2}$ , while extended AGN outflows are less observed. At  $L_{\text{bol}} \gtrsim 10^{46} \text{ erg s}^{-1}$ ,  $f_{\text{Edd,dust}} > 1$  accretion (solid line) may likewise clear the nuclear obscuration, but the high fraction of obscured quasars in the forbidden region suggests a short luminous quasar timescale or an extended,  $\sim 10^{2-3} \text{ pc}$  scale obscuration being cleared slowly by outflows (dotted line).

producing extended outflows at  $f_{\text{Edd,dust}} > 1$  values. We summarize our discussion in Figure 6.

## 7. Summary

Using a collection of AGN samples spanning a wide dynamic range of luminosity, obscuration, and redshift, we probed the distribution of obscuration and accretion rate values to comparatively examine the role of radiation pressure in blowing out obscured quasars. We summarize our findings below:

1. The fraction of AGNs in the forbidden zone for radiation pressure,  $\varphi$ , is kept to  $\lesssim 20\%$  for all of the multi-wavelength-selected AGN samples compiled over a wide range of luminosity and redshift, consistent with previous findings that nuclear obscuration is quickly blown away by radiation pressure once the accretion rate exceeds the Eddington limit for dusty gas.
2. This radiation-pressure feedback, that is, the acceleration of nuclear dusty gas, appears limited for luminous, obscured quasars at  $N_H \gtrsim 10^{22} \text{ cm}^{-2}$  or  $E(B - V) \gtrsim 0.2 \text{ mag}$  and  $L_{\text{bol}} \gtrsim 10^{46} \text{ erg s}^{-1}$ , where they show  $\varphi \gtrsim 60\%$  over a wide range of AGN selection wavelengths or amount of obscuration. This may be explained by a combination of shorter luminous quasar lifetimes and extended obscuration cleared by outflows over a longer timescale than to clear the nuclear obscuration.



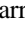





Ultimately, we expect to see the  $M_{\text{BH}}$  values grow while luminous, obscured quasars become unobscured if extended outflows, slower than radiation pressure clearing the nuclear obscuration, are the bottleneck for AGN feedback. Ongoing hard X-ray surveys probing fainter sources (e.g., Lansbury

et al. 2017; Oh et al. 2018) will confirm if distant, gas-obscured quasars are going through similar strengths of radiation-pressure feedback as dust-obscured quasars. Spatially resolved or global  $N_{\text{H}}$  and  $E(B - V)$  estimates for luminous, obscured quasars will better tell whether obscuration is indeed more extended in luminous quasars and will quantify the relative effect of radiation pressure and outflows to their parsec-to-kiloparsec-scale gas and dust environments.

We thank the anonymous referee for the comments that greatly improved the paper and Andrew Fabian for kindly providing the  $f_{\text{Edd,dust}}(N_{\text{H}}) = 1$  curves. This research was supported by the Basic Science Research Program through the National Research Foundation of Korea (NRF) funded by the Ministry of Education (NRF-2017R1A6A3A04005158). R. J.A. was supported by FONDECYT grant No. 1191124. R.C. H. and C.M.C. acknowledge support from the National Science Foundation under CAREER award no. 1554584. C.R. acknowledges support from the Fondecyt Iniciacion grant 11190831.

This work makes use of data from the NuSTAR mission, a project led by Caltech, managed by the Jet Propulsion Laboratory, and funded by NASA. This research has made use of data and/or software provided by the High Energy Astrophysics Science Archive Research Center (HEASARC), which is a service of the Astrophysics Science Division at NASA/GSFC and the High Energy Astrophysics Division of the Smithsonian Astrophysical Observatory. This publication makes use of data products from the United Kingdom Infrared Deep Sky Survey. UKIRT is owned by the University of Hawaii (UH) and operated by the UH Institute for Astronomy; operations are enabled through the cooperation of the East Asian Observatory. When the data reported here were acquired, UKIRT was operated by the Joint Astronomy Centre on behalf of the Science and Technology Facilities Council of the U.K. This publication makes use of data products from the Wide-field Infrared Survey Explorer, which is a joint project of the University of California, Los Angeles, and the Jet Propulsion Laboratory/California Institute of Technology, funded by the National Aeronautics and Space Administration.

### ORCID iDs

Hyunsung D. Jun  <https://orcid.org/0000-0003-1470-5901>  
 Roberto J. Assef  <https://orcid.org/0000-0002-9508-3667>  
 Christopher M. Carroll  <https://orcid.org/0000-0003-3574-2963>  
 Ryan C. Hickox  <https://orcid.org/0000-0003-1468-9526>  
 Yonghui Kim  <https://orcid.org/0000-0003-4164-5414>  
 Jaehyun Lee  <https://orcid.org/0000-0002-6810-1778>  
 Claudio Ricci  <https://orcid.org/0000-0001-5231-2645>  
 Daniel Stern  <https://orcid.org/0000-0003-2686-9241>

### References

- Alexander, D. M., Bauer, F. E., Chapman, S. C., et al. 2005, *ApJ*, 632, 736  
 Alexander, D. M., Brandt, W. N., Smail, I., et al. 2008, *AJ*, 135, 1968  
 Assef, R. J., Brightman, M., Walton, D. J., et al. 2020, *ApJ*, 897, 112  
 Assef, R. J., Eisenhardt, P. R. M., Stern, D., et al. 2015, *ApJ*, 804, 27  
 Assef, R. J., Walton, D. J., Brightman, M., et al. 2016, *ApJ*, 819, 111  
 Baek, J., Chung, A., Schawinski, K., et al. 2019, *MNRAS*, 488, 4317  
 Ballantyne, D. R., Ross, R. R., & Fabian, A. C. 2001, *MNRAS*, 327, 10  
 Banerji, M., Alaghband-Zadeh, S., Hewett, P. C., & McMahon, R. G. 2015, *MNRAS*, 447, 3368  
 Banerji, M., McMahon, R. G., Hewett, P. C., et al. 2012, *MNRAS*, 427, 2275  
 Banerji, M., McMahon, R. G., Hewett, P. C., Gonzalez-Solares, E., & Kposov, S. E. 2013, *MNRAS*, 429, L55  
 Barthelmy, S. D., Barbier, L. M., Cummings, J. R., et al. 2005, *SSRv*, 120, 143  
 Baumgartner, W. H., Tueller, J., Markwardt, C. B., et al. 2013, *ApJS*, 207, 19  
 Bennert, V. N., Auger, M. W., Treu, T., et al. 2011, *ApJ*, 742, 107  
 Bentz, M. C., Denney, K. D., Grier, C. J., et al. 2013, *ApJ*, 767, 149  
 Bentz, M. C., & Katz, S. 2015, *PASP*, 127, 67  
 Bentz, M. C., Peterson, B. M., Netzer, H., et al. 2009, *ApJ*, 697, 160  
 Blain, A. W., Smail, I., Ivison, R. J., et al. 2002, *PhR*, 369, 111  
 Bohlin, R. C., Savage, B. D., & Drake, J. F. 1978, *ApJ*, 224, 132  
 Bongiorno, A., Maiolino, R., Brusa, M., et al. 2014, *MNRAS*, 443, 2077  
 Brightman, M., Baloković, M., Stern, D., et al. 2015, *ApJ*, 805, 41  
 Brightman, M., Masini, A., Ballantyne, D. R., et al. 2016, *ApJ*, 826, 93  
 Brightman, M., & Nandra, K. 2011, *MNRAS*, 413, 1206  
 Buchner, J., & Bauer, F. E. 2017, *MNRAS*, 465, 4348  
 Burscher, L., Davies, R. I., Graciá-Carpio, J., et al. 2016, *A&A*, 586, A28  
 Chen, K., & Halpern, J. P. 1989, *ApJ*, 344, 115  
 Collin, S., Kawaguchi, T., Peterson, B. M., & Vestergaard, M. 2006, *A&A*, 456, 75  
 Corral, A., Georgantopoulos, I., Comastri, A., et al. 2016, *A&A*, 592, A109  
 Dey, A., Soifer, B. T., Desai, V., et al. 2008, *ApJ*, 677, 943  
 Diaz-Santos, T., Assef, R. J., Blain, A. W., et al. 2018, *Sci*, 362, 1034  
 Ding, X., Silverman, J., Treu, T., et al. 2020, *ApJ*, 888, 37  
 Du, P., Hu, C., Lu, K.-X., et al. 2014, *ApJ*, 782, 45  
 Eisenhardt, P. R. M., Wu, J., Tsai, C.-W., et al. 2012, *ApJ*, 755, 173  
 Eracleous, M., & Halpern, J. P. 1994, *ApJS*, 90, 1  
 Ezhikode, S. H., Gandhi, P., Done, C., et al. 2017, *MNRAS*, 472, 3492  
 Fabian, A. C., Celotti, A., & Erlund, M. C. 2006, *MNRAS*, 373, L16  
 Fabian, A. C., Vasudevan, R. V., & Gandhi, P. 2008, *MNRAS*, 385, L43  
 Fabian, A. C., Vasudevan, R. V., Mushotzky, R. F., et al. 2009, *MNRAS*, 394, L89  
 Fan, L., Han, Y., Nikutta, R., et al. 2016, *ApJL*, 822, L32  
 Fiore, F., Feruglio, C., Shankar, F., et al. 2017, *A&A*, 601, A143  
 Fluetsch, A., Maiolino, R., Carniani, S., et al. 2019, *MNRAS*, 483, 4586  
 Gehrels, N., Chincarini, G., Giommi, P., et al. 2004, *ApJ*, 611, 1005  
 Glikman, E. 2017a, *RNAAS*, 1, 48  
 Glikman, E., Helfand, D. J., White, R. L., et al. 2007, *ApJ*, 667, 673  
 Glikman, E., Lacy, M., LaMassa, S., et al. 2018, *ApJ*, 861, 37  
 Glikman, E., LaMassa, S., Piconcelli, E., Urry, M., & Lacy, M. 2017b, *ApJ*, 847, 116  
 Glikman, E., Simmons, B., Mailly, M., et al. 2015, *ApJ*, 806, 218  
 Glikman, E., Urrutia, T., Lacy, M., et al. 2012, *ApJ*, 757, 51  
 Goulding, A. D., Zakamska, N. L., Alexandroff, R. M., et al. 2018, *ApJ*, 856, 4  
 Greene, J. E., Alexandroff, R., Strauss, M. A., et al. 2014, *ApJ*, 788, 91  
 Hamann, F., Zakamska, N. L., Ross, N., et al. 2017, *MNRAS*, 464, 3431  
 Harrison, C. M., Alexander, D. M., Mullaney, J. R., Swinbank, A. M., et al. 2014, *MNRAS*, 330, 441  
 Harrison, F. A., Craig, W. W., Christensen, F. E., et al. 2013, *ApJ*, 770, 103  
 Heckman, T. M., Kauffmann, G., Brinchmann, J., et al. 2004, *ApJ*, 613, 109  
 Hickox, R. C., & Alexander, D. M. 2018, *ARA&A*, 56, 625  
 Hickox, R. C., Jones, C., Forman, W. R., et al. 2009, *ApJ*, 696, 891  
 Ho, L. C., Filippenko, A. V., & Sargent, W. L. W. 1997, *ApJS*, 112, 315  
 Hopkins, P. F., & Elvis, M. 2010, *MNRAS*, 401, 7  
 Hopkins, P. F., & Hernquist, L. 2009, *ApJ*, 698, 1550  
 Hopkins, P. F., Hernquist, L., Cox, T. J., et al. 2006, *ApJS*, 163, 1  
 Hopkins, P. F., Hernquist, L., Cox, T. J., & Kereš, D. 2008, *ApJS*, 175, 356  
 Hopkins, P. F., Hernquist, L., Martini, P., et al. 2005, *ApJL*, 625, L71  
 Ichikawa, K., Ricci, C., Ueda, Y., et al. 2019, *ApJ*, 870, 31  
 Ishibashi, W., Banerji, M., & Fabian, A. C. 2017, *MNRAS*, 469, 1496  
 Ishibashi, W., & Fabian, A. C. 2015, *MNRAS*, 451, 93  
 Ishibashi, W., Fabian, A. C., Ricci, C., et al. 2018, *MNRAS*, 479, 3335  
 Jaffe, W., Meisenheimer, K., Röttgering, H. J. A., et al. 2004, *Natur*, 429, 47  
 Jun, H. D., Assef, R. J., Bauer, F. E., et al. 2020, *ApJ*, 888, 110  
 Jun, H. D., & Im, M. 2013, *ApJ*, 779, 104  
 Jun, H. D., Im, M., Kim, D., & Stern, D. 2017, *ApJ*, 838, 41  
 Jun, H. D., Im, M., Lee, H. M., et al. 2015, *ApJ*, 806, 109  
 Kang, D., & Woo, J.-H. 2018, *ApJ*, 864, 124  
 Kang, D., Woo, J.-H., & Bae, H.-J. 2017, *ApJ*, 845, 131  
 Kauffmann, G., Heckman, T. M., Tremonti, C., et al. 2003, *MNRAS*, 346, 1055  
 Kim, D., & Im, M. 2018, *A&A*, 610, A31  
 Kim, D., Im, M., Glikman, E., Woo, J.-H., & Urrutia, T. 2015, *ApJ*, 812, 66  
 Kim, D., Im, M., & Kim, M. 2010, *ApJ*, 724, 386  
 King, A. 2003, *ApJL*, 596, L27  
 Kishimoto, M., Antonucci, R., Blaes, O., et al. 2008, *Natur*, 454, 492  
 Kishimoto, M., Hönig, S. F., Antonucci, R., et al. 2011, *A&A*, 536, A78

- Kormendy, J., & Ho, L. C. 2013, *ARA&A*, 51, 511
- Koss, M., Trakhtenbrot, B., Ricci, C., et al. 2017, *ApJ*, 850, 74
- Krimm, H. A., Holland, S. T., Corbet, R. H. D., et al. 2013, *ApJS*, 209, 14
- Lacy, M., Ridgway, S. E., Sajina, A., et al. 2015, *ApJ*, 802, 102
- LaMassa, S. M., Glikman, E., Brusa, M., et al. 2017, *ApJ*, 847, 100
- LaMassa, S. M., Ricarte, A., Glikman, E., et al. 2016, *ApJ*, 820, 70
- Lansbury, G. B., Alexander, D. M., Aird, J., et al. 2017, *ApJ*, 846, 20
- Lansbury, G. B., Banerji, M., Fabian, A. C., et al. 2020, *MNRAS*, 495, 2652
- Lawrence, A. 1991, *MNRAS*, 252, 586
- Lawrence, A., Warren, S. J., Almaini, O., et al. 2007, *MNRAS*, 379, 1599
- Liu, Y., & Li, X. 2015, *MNRAS*, 448, L53
- Lusso, E., Comastri, A., Simmons, B. D., et al. 2012, *MNRAS*, 425, 623
- Maiolino, R., Marconi, A., Salvati, M., et al. 2001, *A&A*, 365, 28
- Maiolino, R., Risaliti, G., Salvati, M., et al. 2010, *A&A*, 517, A47
- Maiolino, R., Shemmer, O., Imanishi, M., et al. 2007, *A&A*, 468, 979
- Marconi, A., Risaliti, G., Gilli, R., et al. 2004, *MNRAS*, 351, 169
- Martini, P. 2004, in *Coevolution of Black Holes and Galaxies*, ed. L. C. Ho, Vol. 169 (Cambridge: Cambridge Univ. Press)
- Martocchia, S., Piconcelli, E., Zappacosta, L., et al. 2017, *A&A*, 608, A51
- Massaro, E., Maselli, A., Leto, C., et al. 2015, *Ap&SS*, 357, 75
- Merloni, A., Bongiorno, A., Brusa, M., et al. 2014, *MNRAS*, 437, 3550
- Minezaki, T., Yoshii, Y., Kobayashi, Y., et al. 2019, *ApJ*, 886, 150
- Murphy, K. D., & Yaqoob, T. 2009, *MNRAS*, 397, 1549
- Murray, N., Quataert, E., & Thompson, T. A. 2005, *ApJ*, 618, 569
- Oh, K., Koss, M., Markwardt, C. B., et al. 2018, *ApJS*, 235, 4
- Osterbrock, D. E. 1979, *AJ*, 84, 901
- Pâris, I., Petitjean, P., Aubourg, É., et al. 2012, *A&A*, 548, A66
- Park, K., & Ricotti, M. 2011, *ApJ*, 739, 2
- Perrotta, S., Hamann, F., Zakamska, N. L., et al. 2019, *MNRAS*, 488, 4126
- Peterson, B. M., Ferrarese, L., Gilbert, K. M., et al. 2004, *ApJ*, 613, 682
- Rakshit, S., & Woo, J.-H. 2018, *ApJ*, 865, 5
- Ramos Almeida, C., & Ricci, C. 2017, *NatAs*, 1, 679
- Ricci, C., Assef, R. J., Stern, D., et al. 2017a, *ApJ*, 835, 105
- Ricci, C., Bauer, F. E., Treister, E., et al. 2017b, *MNRAS*, 468, 1273
- Ricci, C., Trakhtenbrot, B., Koss, M. J., et al. 2017c, *Natur*, 549, 488
- Ricci, C., Trakhtenbrot, B., Koss, M. J., et al. 2017d, *ApJS*, 233, 17
- Richards, G. T., Lacy, M., Storrie-Lombardi, L. J., et al. 2006, *ApJS*, 166, 470
- Rigby, J. R., Diamond-Stanic, A. M., & Aniano, G. 2009, *ApJ*, 700, 1878
- Risaliti, G., Elvis, M., Fabbiano, G., et al. 2007, *ApJL*, 659, L111
- Risaliti, G., Elvis, M., & Nicastro, F. 2002, *ApJ*, 571, 234
- Ross, N. P., Hamann, F., Zakamska, N. L., et al. 2015, *MNRAS*, 453, 3932
- Sanders, D. B., & Mirabel, I. F. 1996, *ARA&A*, 34, 749
- Sanders, D. B., Soifer, B. T., Elias, J. H., et al. 1988, *ApJ*, 325, 74
- Schneider, D. P., Richards, G. T., Hall, P. B., et al. 2010, *AJ*, 139, 2360
- Sérsic, J. L. 1963, *BAAA*, 6, 41
- Severgnini, P., Risaliti, G., Marconi, A., Maiolino, R., & Salvati, M. 2001, *A&A*, 368, 44
- Shakura, N. I., & Sunyaev, R. A. 1973, *A&A*, 24, 337
- Shen, Y., & Ho, L. C. 2014, *Natur*, 513, 210
- Shen, Y., Richards, G. T., Strauss, M. A., et al. 2011, *ApJS*, 194, 45
- Shin, J., Woo, J.-H., Chung, A., et al. 2019, *ApJ*, 881, 147
- Stern, D., Lansbury, G. B., Assef, R. J., et al. 2014, *ApJ*, 794, 102
- Suh, H., Civano, F., Trakhtenbrot, B., et al. 2020, *ApJ*, 889, 32
- Tacconi, L. J., Genzel, R., Neri, R., et al. 2010, *Natur*, 463, 781
- Temple, M. J., Banerji, M., Hewett, P. C., et al. 2019, *MNRAS*, 487, 2594
- Thompson, T. A., Fabian, A. C., Quataert, E., et al. 2015, *MNRAS*, 449, 147
- Toba, Y., Bae, H.-J., Nagao, T., et al. 2017, *ApJ*, 850, 140
- Toba, Y., Oyabu, S., Matsuhara, H., et al. 2014, *ApJ*, 788, 45
- Toba, Y., Yamada, S., Ueda, Y., et al. 2020, *ApJ*, 888, 8
- Treister, E., Schawinski, K., Urry, C. M., et al. 2012, *ApJL*, 758, L39
- Tsai, C.-W., Eisenhardt, P. R. M., Wu, J., et al. 2015, *ApJ*, 805, 90
- Urrutia, T., Becker, R. H., White, R. L., et al. 2009, *ApJ*, 698, 1095
- Urrutia, T., Lacy, M., & Becker, R. H. 2008, *ApJ*, 674, 80
- Urrutia, T., Lacy, M., Spoon, H., et al. 2012, *ApJ*, 757, 125
- Usman, S. M., Murray, S. S., Hickox, R. C., et al. 2014, *ApJL*, 788, L3
- Vasudevan, R. V., & Fabian, A. C. 2007, *MNRAS*, 381, 1235
- Vietri, G., Piconcelli, E., Bischetti, M., et al. 2018, *A&A*, 617, A81
- Vito, F., Brandt, W. N., Stern, D., et al. 2018, *MNRAS*, 474, 4528
- Winkler, H. 1992, *MNRAS*, 257, 677
- Woo, J.-H., Bae, H.-J., Son, D., & Karouzos, M. 2016, *ApJ*, 817, 108
- Woo, J.-H., Yoon, Y., Park, S., et al. 2015, *ApJ*, 801, 38
- Wu, J., Jun, H. D., Assef, R. J., et al. 2018, *ApJ*, 852, 96
- Yajima, H., Ricotti, M., Park, K., et al. 2017, *ApJ*, 846, 3
- Young, M., Elvis, M., & Risaliti, G. 2009, *ApJS*, 183, 17
- Zakamska, N. L., Schmidt, G. D., Smith, P. S., et al. 2005, *AJ*, 129, 1212
- Zakamska, N. L., Strauss, M. A., Krolik, J. H., et al. 2003, *AJ*, 126, 2125
- Zappacosta, L., Piconcelli, E., Duras, F., et al. 2018, *A&A*, 618, A28